Updated Magnetostratigraphy for The Eocene Green River Formation, Wyoming

A THESIS
SUBMITTED TO THE FACULTY OF THE GRADUATE SCHOOL OF
THE UNIVERSITY OF MINNESOTA
BY

Emma Lincoln Schneider

IN PARTIAL FULFILLMENT OF THE REQUIREMENTS FOR THE
DEGREE OF MASTER OF SCIENCE

Joshua M. Feinberg

May, 2022

Acknowledgements

I am deeply thankful for all the support I received as I wrote this thesis. First and foremost, my advisor Josh Feinberg has been an incredible mentor. Over the course of my Master's degree, he has guided me through equipment failures, a pandemic, personal losses, and career exploration. His unwavering support and kindness truly made my work possible, and I hope he enjoyed working together as much as I did.

I was lucky to work with some incredible scholars along the way. I found my footing in the Green River Formation thanks to Mike Smith and Alan Carroll and their lifetimes of knowledge. Our project was greatly improved by collaboration with Brad Singer, Ben Bruck, and Mark David Schmitz, as well as the rest of the GREECO Team who provided data and interdisciplinary knowledge. I'm thankful for everyone at the Institute for Rock Magnetism as their patience and skill allowed me to collect accurate and valuable data right from the start, in particular Peat Solheid and Dario Bilardello, who always carved time out of their day to teach me or fix a broken machine. I'm thankful to Julie Bowles, who graciously allowed me to use her paleomagnetism lab at University of Wisconsin-Milwaukee for crucial samples while my usual machines were being repaired. Finally, throughout my graduate education I was fortunate to be guided and encouraged by my friends in Josh's research group including Rashida Doctor, Kathryn Hobart, John McDaris, and Josie Welsh, as well as my fellow graduate students in the Earth & Environmental Sciences Department.

My work would not have been possible without the love and support of my family and friends. My partner, my parents, my brother, my dear friends, and my extended family brought joy and purpose to my life through the challenges and triumphs of the past three years. As I finish this thesis, I think of my grandparents, as they always supported my education and couldn't all make it to see me graduate.

Our project was conducted on the traditional territory of the Ute, Eastern Shoshone, Shoshone - Bannock, and Cheyenne people.

Abstract

The Green River Formation (GRF) is one of the best-preserved continuous Eocene terrestrial records in the world, allowing researchers to track phenomena in high resolution related to climate, vegetation, tectonics, and geomorphology. The preservation of the early Eocene in the GRF is particularly important as it records the Early Eocene Climatic Optimum (EECO), an analog for current greenhouse gas-driven global warming. Here we provide an updated magnetostratigraphy for the Wilkins Peak Member (WPM) of the GRF integrated with recent ^{238}U-^{206}Pb and $^{40}Ar/^{39}Ar$ results that more confidently identifies the geomagnetic reversals preserved in the sediments (C22n, C22r, C23n.1n, C23n1.1r, C23n.2n, and C23r) and refines their radioisotopic ages. Earlier GRF magnetostratigraphic studies were challenged by the presence of pervasive authigenic pyrrhotite in sediments of the Wilkins Peak member (Sheriff and Shive, 1982), which are confirmed in non-tuff lithologies in this study. Here, we build on the work of Tsukui and Clyde (2012) by focusing paleomagnetic sampling on ash-fall tuffs, which are more resistant to the formation of authigenic sulfides and can be dated directly using ^{238}U-^{206}Pb and $^{40}Ar/^{39}Ar$ techniques. The tuffs were deposited in a closed-lake basin setting and are sufficient in number to refine the stratigraphic position of geomagnetic reversals. Most tuffs show minimal post-depositional alteration and act as reliable paleomagnetic recorders. Tuffs of both normal and reversed polarity were identified using alternating field and thermal demagnetization protocols. The magnetic mineral carriers are magnetite, hematite, and their Ti-substituted equivalents and were characterized using hysteresis loops, backfield curves, and magnetic susceptibility. Fe-sulfides are present in some samples and produce secondary magnetic minerals during thermal demagnetization at temperatures >450°C. This updated terrestrial magnetostratigraphy provides an important bridge for correlating to marine records deposited across the EECO, and ongoing cyclostratigraphic work promises an even higher resolution view of the natural history preserved within the GRF.

Contents

List of Tables

List of Figures

INTRODUCTION

The Early Eocene Climatic Optimum (EECO) occurred approximately 53 - 50 Ma and features the Earth's hottest prolonged temperatures across the entire Cenozoic. The EECO has been associated with elevated levels of atmospheric CO_2 (Greenwood and Wing, 1995; Zachos et al., 2001; Pearson et al., 2001; Zhu et al., 2019), and hence, this period has been suggested as a proxy for understanding modern climate change (Clyde et al., 2001; Lowenstein and Demicco, 2006; Zachos et al., 2008). Efforts to compare effects of the EECO across marine and terrestrial settings are hampered by sparse radioisotopic dates and large uncertainties (Vandenberghe et al., 2012). Environmental changes related to the EECO have been observed globally (Wilf et al., 2003; Ivany et al., 2008), but the quality of marine records of such hyperthermals are impacted by low oceanic pH due to high carbon levels, leading to carbonate dissolution and condensed deposits (Westerhold and Roehl, 2009; Lauretano et al., 2018). In contrast, continental basins provide comparatively expanded and detailed records of this time (Roehler, 1992; Chamberlain et al., 2013; Smith et al., 2014) preserving evidence of dramatic shifts in regional climate, sediment input, and fossil assemblages (Clyde et al., 1997, 2001; Sewall and Sloan, 2006; Woodburne et al., 2009; Hyland and Sheldon, 2013). The Green River Formation (GRF), WY, USA is one such basin sequence. The GRF's Wilkins Peak member was deposited across the EECO and represents an alkaline lake environmental setting (pH > 10) (Jagniecki and Lowenstein, 2015). This study provides an updated magnetostratigraphy of the Wilkins Peak member, thereby allowing researchers to use the Geomagnetic Polarity Time Scale (GPTS) to correlate terrestrial records of the EECO with the marine paleoclimate archive. The sequence of geomagnetic field reversals described by the GPTS provides chronologic tie-points in the rock record that transcend terrestrial and marine depositional settings. Additionally, recent $^{40}Ar/^{39}Ar$ and U-Pb radioisotopic ages of ash layers within the GRF may allow us to further refine the ages of geomagnetic reversals and improve the accuracy of the GPTS for future researchers.

GEOLOGIC CONTEXT

Depositional setting of the Green River Formation

The Green River Formation is a group of associated lacustrine and alluvial sedimentary facies that provides one of the most complete stratigraphic records of the early-middle Eocene in the world (Bradley, 1964; Sullivan, 1980; Roehler, 1992; Murphey, 2001). The GRF was primarily deposited in Laramide basins in what is now northeastern Utah, northwestern Colorado, and southwestern Wyoming that are bounded by uplifts (Fig. 1). Samples used in this study were collected primarily within the Greater Green River Basin. The Bridger-Washakie and Wasatch Formations were deposited in these basins above and below the GRF, respectively (Bradley, 1964; Sullivan, 1980). The GRF is further divided from oldest to youngest into the Laney, Wilkins Peak, and Tipton Members, which generally represent different lacustrine depositional environments (Smith et al., 2008). Broadly, the GRF is composed primarily of lacustrine and alluvial facies of finely laminated shale with thick facies of limestone, sandstone, and paleosols interspersed with evaporites and ash-fall tuffs (Murphey, 2001). The lithologies cycle in tandem with orbital eccentricity (Aswasereelert et al., 2013). The Wilkins Peak Member (WPM) is of particular interest as it records the majority of the EECO and contains economically important oil shales and sodium carbonate evaporites, specifically trona, deposited in an under-filled evaporitic lake basin (Ratterman et al., 1981; Smith et al., 2008; Jagniecki and Lowenstein, 2015). Nine distinct alluvial facies labeled marker beds A-I (Culbertson, 1961; Pietras and Carroll, 2006) are interspersed within lacustrine sediments of the WPM, aiding both magneto- and cyclo-stratigraphy. The GRF and the WPM specifically is therefore an excellent high-resolution archive of the early-middle Eocene, especially across the EECO (Frantz et al., 2014).

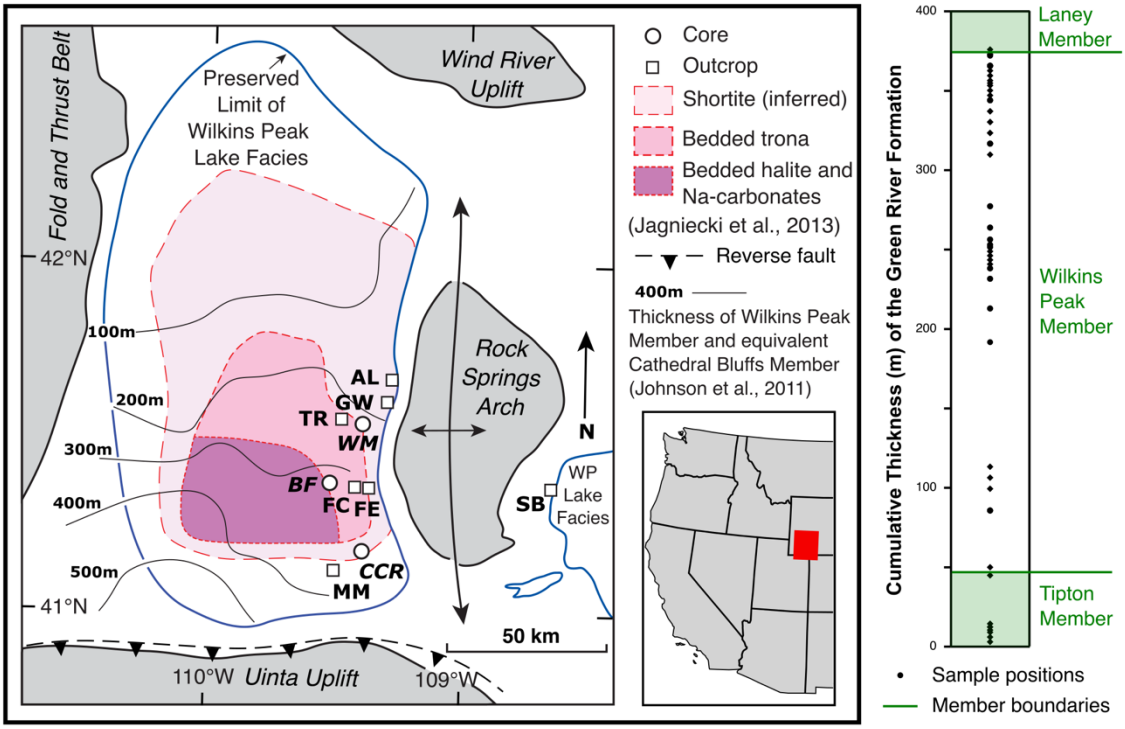

Figure 1. Simplified geologic map of the extent of the Wilkins Peak Member of the Green River Formation (GRF) and equivalent Cathedral Bluffs Member in the Bridger Basin, with stratigraphic position of samples (small black circles) within the GRF shown in the simplified stratigraphy on the right. Squares indicate outcrops sampled for this study with abbreviated names as seen in Table 1; AL: Apache Lane, FC: Firehole Canyon, FE: Firehole Canyon East, GW: Gookin - White Mountain Road, MM: Middle Marsh Creek Syncline, SB: Sand Butte, TR: Tollgate Rock. Open circles indicate core locations with abbreviated names; BF: ERDA-LERC Blacks Fork 1, CCR: U.S. DOE/LETC Currant Creek Ridge-1, WM: White Mountain. Figure after Bruck et al. (2020) with data from Johnson et al. (2011) and Jagniecki et al. (2013).

Existing geochronology of the GRF

The GRF provides an ideal section in which to study the EECO due to preservation of its fine-scale sedimentary features and relatively continuous deposition. The most complete model describing the chronology of the GRF (Smith et al., 2014) uses tiered interpolation (TI) to combine radioisotopic ages (Smith et al., 2008, 2010), paleomagnetic data (Clyde et al., 1997, 2001; Tsukui and Clyde, 2012), mammalian biostratigraphy (Clyde et al., 1997, 2001; Zonneveld et al., 2000; Smith et al., 2008) and geochemistry (Clyde et al., 2001; Westerhold and Roehl, 2009; Hyland and Sheldon, 2013). The TI model correlates between spatially and temporally broad sections in an attempt to ensure reliability throughout the GRF. However, efforts to identify and integrate geomagnetic reversals into the Wilkins Peak Member often require making extrapolations from sites far outside the main Green River Basin, thereby introducing ambiguity that is difficult to resolve. The recent production of new radioisotopic ages from tuffs within the Wilkins Peak Member (Bruck et al., 2020; 2021) combined with the publication of the most recent Geomagnetic Polarity Timescale (GPTS) (Ogg, 2020) provides an opportunity to test and refine previous magnetostratigraphic models of the GRF. Additionally, this higher-resolution GRF magnetostratigraphy may help resolve long-standing discrepancies (cf. Smith et al., 2014; Westerhold et al., 2015) and lead to better correlation with marine data spanning the EECO, stronger controls on sediment accumulation rates and climate fluctuations, and possible adjustment of the ages of chrons in the GPTS.

Previous paleomagnetic work

Previous paleomagnetic studies of the Green River Formation provide valuable context and direction for our study. The first GRF paleomagnetic study was conducted by Strangway & McMahon (1973), who demonstrated that sediments from a 10 m section of the Parachute Creek member near Piceance Creek retained meaningful directions obtained after alternating field demagnetization up to 10 mT with remanence measured using a spinner magnetometer. They emphasized the weak magnetization of the samples and estimated magnetite with a concentration of 2 ppm as the primary magnetic

recorder. Next, Hallan Noltimier of Ohio State University advised a series of undergraduate theses focusing on the paleomagnetism of oil shales connected to the GRF. Their work showed that magnetizations from Piceance Creek basin oil shales could be measured accurately even after 40 mT (Karoly, 1974). Fugitt (1976) determined a paleomagnetic pole and identified a geomagnetic reversal in the oil shales of the closely related North Horn Formation in Utah. Additional geomagnetic reversals were identified by students of Noltimier within a core through the Mahogany Oil shale from Duchesne Co., Utah in the Uinta basin (Fenzan, 1978; Richardson, 1980). These latter studies represent the first time a superconducting magnetometer was used to analyze GRF materials and the identified reversals were correlated to the GPTS. Shortly thereafter, Sheriff and Shive (1982) demonstrated that the primary magnetic mineral in organic rich oil shales of the Wilkins Peak Member was authigenic pyrrhotite and argued that meaningful paleomagnetic data would be difficult to obtain from these samples. This work cast doubt on the reliability of the earlier studies and impaired further paleomagnetic research on the GRF for the next decade.

The early 1990s ushered some new paleomagnetic research on the GRF, although it was focused primarily on establishing its lower age, including work on the Willwood Formation (Wing et al., 1991; Clyde et al., 1994; Tauxe et al., 1994). The next two decades of paleomagnetic work on the GRF were led by William Clyde and his colleagues. The first modern paleomagnetic study of the Green River Formation was presented by Clyde et al. (1997) and involved the use of both alternating field and thermal demagnetization protocols as well as principal component analysis to isolate characteristic remanence directions and identify secondary components. Much of this initial work focused on correlating the magnetization of paleosols, formed on mudstone deposits in the Wasatch Formation as well as on marly limestones in the Wilkins Peak Member of the GRF, with the GPTS and fossil record. The study found evidence of secondary mineral growth in the form of goethite and demonstrated that paleosols could yield reliable results, while limestones were far less faithful paleomagnetic recorders. Work on paleosols continued in Clyde et al. (2001), which constrained the position of the Wasatchian/Bridgerian boundary to within chron C23r at about 52 Ma, about 2 Ma older than previously estimated. It was noted again that the Green River Formation sediments

showed unusually weak remanences compared to those in the underlying Wasatch and overlying Bridger Formations (Sheriff and Shive, 1982; Clyde et al., 1997). Finally, a major breakthrough occurred when Tsukui and Clyde targeted the ash-fall tuffs that occur throughout the GRF (2012). They measured the paleodirections recorded by 19 ash-fall tuffs (120 specimens) from within the Green River Formation and combined their results with previously established $^{40}Ar/^{39}Ar$ ages (Smith et al., 2008). While the sediments of the GRF were weak and prone to alteration, the ash fall tuffs were shown to be slightly more magnetic and less altered by diagenetic processes, thereby providing high quality snapshots of geomagnetic polarity throughout the GRF. The ashes were assumed to have cooled during transport and recorded a depositional remanent magnetization as they were deposited into the lacustrine setting of the Wilkins Peak member. This methodology allowed Tsukui and Clyde (2012) to compare several age models and refine the magnetostratigraphy of the full GRF. This approach is the inspiration for this study, where we aim to greatly expand the number and variety of units tested within the Wilkins Peak member of the GRF, precisely determine the stratigraphic positions that record reversals, and use more advanced radioisotopic techniques to more precisely date each tuff.

Ash-fall tuff deposition & lithology

While the GRF contains a wide variety of lithologies, this study focuses primarily on ash-fall tuffs that occur throughout the majority of the formation. The tuffs originate from volcanic activity in the Absaroka Range and Challis volcanic fields to the northwest of the GRF in Wyoming and Idaho (Bradley, 1964; Chetel et al., 2011). The tuff beds are composed largely of volcaniclastics ranging in composition between andesitic and rhyolitic (Bradley, 1964) [A49-50] and from clay to fine sand in grain size (Tsukui and Clyde, 2012). The tuffs are intercalated with lacustrine strata, primarily mudstone and limestone. Some of the tuffs were subsequently reworked into tuffaceous carbonates and mudstones, occasionally making it difficult to distinguish a ‘true’ tuff. However, as the tuffs settled rapidly in lakes, their composition is largely uniform throughout individual beds with identifiable, discrete surfaces (Bradley, 1964). Biotite crystals are observed in

many ash-fall tuffs to grade upward to finer grain sizes, further supporting their deposition during a single event. This depositional rapidity suggests that each tuff should record a single polarity at the time of deposition and highlights the tuffs as temporally constrained marker units (Tsukui and Clyde, 2012).

Ash-fall tuff as choice for paleomagnetic work

This study employs ash-fall tuffs as the signature paleomagnetic recorder for the GRF. The tuffs often stand out visually in outcrop as they are usually more competent, cohesive, and more thickly bedded than surrounding strata, and show less evidence of alteration (Tsukui and Clyde, 2012). They range from white to gray to orange in color. Many tuffs in the Wilkins Peak member have informal names and are laterally continuous with distinct contacts, explaining their use as recognizable marker beds within the formation and providing clear tie points for radiometric dates (Clyde et al., 2001; Bruck et al., 2020). Although most tuffs do not show evidence of post-depositional reworking, there is evidence of secondary and even tertiary mineral alteration, including zeolitization (Griggs, 1968; Ratterman et al., 1981). Here, we pay special attention to the magnetic mineral assemblage in each tuff to address concerns related to post-depositional remanence acquisition. The depositional remanent magnetization (DRM) mechanism by which water-lain ash acquires a remanence is relatively well understood (Reynolds, 1979; Hayashida et al., 1996; Iwaki and Hayashida, 2003). The deposition of each tuff was likely a single event (Bradley, 1964; Tsukui and Clyde, 2012), and pilot samples within this study corroborated previous studies (Tsukui and Clyde, 2012), showing that the tuffs are a reliable, if still somewhat weak, paleomagnetic recorder. Although other lithologies were sampled from within the Wilkins Peak member, they are shown to be poor paleomagnetic recorders and are less than useful for magnetostratigraphic studies.

METHODS

Sample collection and preparation

Paleomagnetic samples were collected by several groups during separate field campaigns. The first set of ash-fall tuffs analyzed in this study were collected by Andrew Walters (UW-Madison), including seven tuffs from exposures near Tollgate Rock in 2016 and 23 from outcrops along Gookin-White Mountain Road in 2017. These hand samples were originally collected for ^{40}Ar-3^{9}Ar geochronology and were often azimuthally unoriented. However, every sample includes an orientation mark indicating “up” and occasionally a north arrow, thereby permitting inclination analysis. Six additional samples were collected in the summer of 2019 from various locations listed in Table 1 to test the suitability of different lithologies for paleomagnetic analysis, including shale, marlstone, and ash-fall tuffs. It is important to emphasize the horizontal nature of bedding throughout the Green Formation in this area. None of the strata from which samples were collected between 2016 and 2019 display a dip > 5°. While fully oriented samples are preferred for magnetostratigraphic studies, important polarity information can still be obtained from these samples as we sought to make reasonable progress during a global pandemic. However, the lack of azimuthal and hade information prevents a detailed paleosecular variation or paleogeography analysis of these samples. A final set of fully oriented block samples and drilled cores were collected during the summer of 2020 by ES and JMF with the intent of collecting key untested tuffs and constraining the stratigraphic positions of reversals. 2.5 cm (1 in.) diameter cores were collected using a gas-powered drill and were oriented in place using a Brunton compass and a sun compass when possible.

Hand samples were processed for paleomagnetic analyses at the Institute for Rock Magnetism (IRM), University of Minnesota. Samples were cut into ~2 cm cubes while maintaining orientation and minimizing weathered material. If was not specified on the sample, an arbitrary direction was chosen and preserved for all sub-specimens from a sample. Cores were cut to ~2.25 cm in length. All specimens were sanded to remove

possible magnetic contamination from processing tools. A portion of the unweathered material was gently crushed into powder for ancillary analyses.

Paleomagnetic and analysis procedures

Paleomagnetic analyses were primarily conducted at the IRM (a), University of Minnesota with additional samples run at the Paleomagnetic Lab (b), University of Wisconsin--Milwaukee. Specimens' full vector magnetic remanence was measured using a 2G Enterprises 760-R SQUID magnetometer (a) and a 2G Enterprises 755SRMS Superconducting Rock Magnetometer (b), both of which are within shielded rooms with background fields <300 nT(a). A D-Tech D-2000 (a) and an ASC D-2000 Alternating Field Demagnetizer (b) were used for AF demagnetization while an ASC Scientific TD48-SC furnace (a) and an ASC Thermal Demagnetizer (b) were used for thermal demagnetization.

Three-axis magnetizations were measured after each demagnetization step. Half of the cubed specimens from each sample were progressively demagnetized using an alternating field (AF) sequence of 0, 2, 4, 6, 10, 15, 20, 25, 30, 40, 50, 70, 90, 110, 150, and 170 mT. The second half were progressively demagnetized in temperature steps of 25, 50, 75, 100, 125, 150, 200, 250, 300, 400, 500, 540, 580, 600, 650, and 690°C. Results were first analyzed using PuffinPlot (Lurcock and Wilson, 2012), using unanchored principal component analysis (PCA). Specimen results were considered robust if the maximum angular deviation (MAD) for the PCA was < 20°. Data from specimens with MADs > 20° were not incorporated into further analyses. Mean sample directions were calculated using Fisher means for four or more specimens. Each sample was designated as having either a normal or reversed polarity depending on whether its mean dip was positive or negative, respectively. Samples with dips within ±10° of horizontal are rare and treated with caution during our magnetostratigraphic analysis. These samples are designated with a [1] in Table 1.

In total, this study includes AF and thermal demagnetization results from 565 specimens representing 59 new samples from within the Green River Formation.

The representative magnetic mineralogy of each sample was assessed using a combination of rock magnetic measurements. Curie/Neél temperatures for the constituent magnetic minerals in each sample were identified during measurements of low field magnetic susceptibility as a function of temperature using a Geofyzika KLY-2 KappaBridge AC Susceptibility Bridge with a CS2 furnace (300 A/m and 920 Hz). Measurements were conducted between room temperature and 690°C in air and argon and critical temperatures were identified using the first derivative of magnetic susceptibility. To learn more about each sample's distribution of magnetic grain sizes and concentration of ferromagnetic material, hysteresis loops and backfield curves were measured up to 1 T at room temperature using a Princeton Measurements μMag Vibrating Sample Magnetometer and Lake Shore VSM 8600. To monitor and identify mineral alteration during thermal demagnetization experiments, the low field magnetic susceptibility of each specimen was measured at room temperature after each thermal demagnetization step. These measurements were conducted using a MAGNON Variable Frequency Susceptibility Meter or a Bartington Magnetic Susceptibility Meter MS2 using a 300 A/m field at 2 kHz.

RESULTS

TABLE 1: SUMMARY SITE STATISTICS

Site	Name	Abbrev.	Lithology	Alternate Label	Lat (°)	Long (°)	Location	N	Dec (°)	Inc (°)	*k*	α_{95} (°)
16TR1	Sixth tuff	6	Tuff	2016-14-TR	41.543056	-109.482389	TR	10	1.9	56.0	175.3	3.7
16TR2	-	-	Tuff	2016-13-TR	41.542861	-109.482083	TR	9	338.6	83.1	8.6	18.6
16TR3	Layered tuff	L	Tuff	2016-12-TR	41.542694	-109.482111	TR	10	323.2	59.7	45.7	7.2
16TR4	-	-	Tuff	2016-11-TR	41.542250	-109.482444	TR	4	337.3	54.7	20.6	17.2
16TR5	-	-	Tuff	2016-10-TR	41.542250	-109.482444	TR	5	321.9	63.3	21.7	16.8
16TR6	-	-	Tuff	2016-09-TR	41.542250	-109.482444	TR	6	315.8	64.3	126.1	6
16TR7	Main tuff	M	Tuff	2016-8.1-TR	41.542306	-109.482194	TR	10	333.4	67.3	4.4	26.2
17GW01	Sixth Tuff	6	Tuff	2017-31-GWM	41.589288	-109.309423	GW	9	244.9	64.2	3.3	33.8
17GW02	Sixth Tuff	6	Tuff	2017-32-GWM	41.589247	-109.309391	GW	7	60.4	36.9	1.3	--
17GW03	-	-	Tuff	2017-34-GWM	41.589075	-109.309474	GW	10	248.9	61.1	112.7	4.6
17GW04	Sixth Tuff	6	Tuff	2017-33-GWM	41.589586	-109.308943	GW	10	24.2	40.6	1.4	--
17GW05	-	-	Tuff	2017-35-GWM	41.589566	-109.308798	GW	10	60.0	77.3	3.4	35.8
17GW06	-	-	Tuff	2017-36-GWM	41.589599	-109.308695	GW	8	21.4	65.5	5.8	21.9
17GW07	-	-	Tuff	2017-37-GWM	41.589647	-109.308635	GW	10	342.3	66.4	20.2	11
17GW08	-	-	Tuff	2017-38-GWM	41.589686	-109.308518	GW	10	60.6	58.5	23	10.3
17GW09	-	-	Tuff	2017-39-GWM	41.589658	-109.308490	GW	10	344.5	31.6	16.5	12.3
17GW10	-	-	Tuff	2017-40-GWM	41.589659	-109.308499	GW	5	44.8	70.0	4.5	20.8
17GW11	Layered tuff	L	Tuff	2017-41-GWM	41.589725	-109.308398	GW	10	105.4	82.9	5.3	23.2
17GW13	-	-	Tuff	2017-43-GWM	41.589791	-109.308025	GW	10	239.5	42.3	27.8	9.3
17GW16	- (one below main tuff)	-	Tuff	2017-46-GWM	41.590462	-109.307843	GW	8	264.3	20.3	4.5	29.3
17GW21	Below Second = 22	-	Tuff	2017-51-GWM	41.584802	-109.302625	GW	10	46.7	55.2	21.5	10.7
17GW22	Below Second = 21	-	Tuff	2017-53-GWM	41.585367	-109.301858	GW	10	54.0	58.0	344.7	2.6
17GW23	Firehole	F	Tuff	2017-52-GWM	41.585593	-109.300715	GW	10	303.6	21.2	10.8	15.4
17GW25	Schegg's Candidate	S	Tuff	2017-55-GWM	41.584801	-109.298066	GW	8	4.3	-61.4	68.6	6.7
17GW26	-	-	Tuff	2017-56-GWM	41.584826	-109.297995	GW	8	55.2	-59.2	19.2	13
17GW27	-	-	Tuff	2017-57-GWM	41.584752	-109.297893	GW	10	105.7	-70.5	13.8	13.5
17GW28	-	-	Tuff	2017-58-GWM	41.584731	-109.297677	GW	10	330.8	-56.6	407.1	2.4
19GR1A*	Orange U-rich marker bed	-	Marl	-	41.351586	-109.413169	FE	4	312.5	86.9	92.7	9.6
19GR1B	Orange U-rich marker bed	-	Marl	-	41.351586	-109.413169	FE	4	168.8	-60.5	132.7	8
19GR2*	5' Above Tipton	-	Shale	-	41.347694	-109.379753	FE	8	319.3	65.3	303.1	3.2
19GR3	Firehole Tuff	F	Tuff	-	41.35011	-109.382010	FE	4	33.4	83.1	4.9	46.2
19GR4	Main Tuff	M	Tuff	-	41.542242	-109.482203	TR	8	167.1	34.2	17.3	13.7
19GR5	Above F, Below 2	-	Tuff	-	41.656956	-109.287644	AL	8	199.5	73.9	8.3	20.4
19GR6[1]	Grey Tuff	G	Tuff	-	41.65725	-109.28876	AL	18	239.8	1.6	20.3	7.9
20AL03[1]	Rife Equivalent	R	Tuff	-	41.65643	-109.28652	AL	8	110.4	9.6	10.8	17.6
20MM01	Analcite Tuff	A	Tuff	-	41.10052	-109.50792	MM	10	351.6	73.5	9.5	16.5
20FC02*	Above F-bed	-	Paleosol **	-	41.34804	-109.43028	FC	10	16.6	52.6	7.5	18.9
20FC03*	Above 02	-	Paleosol	-	41.34850	-109.43018	FC	6	144.5	81.4	8.8	23.9
20FC04*	Above 03	-	Sandy Carbonate	-	41.34892	-109.43001	FC	6	190.9	77.2	7	27.2
20FC05*	Above 04	-	Sandstone	-	41.34923	-109.42977	FC	10	4.5	50.5	7.4	19.1
20FC06*	Above 05	-		-	41.34927	-109.42976	FC	10	316.2	49.6	8.9	17.1
20FC07*	Lower G-bed	-	Sandstone	-	41.34948	-109.42952	FC	10	233.6	45.3	96.3	4.9
20FC08*	Middle G-bed	-		-	41.34970	-109.42937	FC	10	327.0	67.0	8.6	17.4
20FC09*	Larger beds w/in G-bed	-	Paleosol	-	41.34983	-109.42931	FC	10	3.7	64.5	268.2	3
20FC11	H-bed	-	Sandstone	-	41.35019	-109.42908	FC	8	295.5	22.7	3.9	32.2

* Samples do not preserve original direction
[1] Samples with dips within ±10° of horizontal
N the number of samples used to determine paleomagnetic polarity
k precision parameter
α_{95} cone of 95% confidence about estimated mean direction
Location key: TR: Tollgate Rock, GW: Gookin-White Mtn Rd, FE: Firehole Canyon East, AL: Apache Lane, MM: Mid Marsh Creek Syncline, FC: Firehole Canyon Section

Natural Remanent Magnetization, NRM

Table 1 lists average NRM intensities for all paleomagnetic sites investigated in this study, and interested readers are encouraged to examine specimen-level data from the MagIC datafile associated with this study. In total, 44 samples from paleomagnetic sites were demagnetized using both thermal and alternating field demagnetization methods, resulting in a total of 421 usable specimens. A wide range of NRM intensities were observed ranging from 7.50×10^{-9} to 3.74×10^{-5} Am^2/kg. The average NRM intensity was relatively weak, 1.10×10^{-6} Am^2/kg, which meant that some more weakly magnetized specimens were near the sensitivity of the 2G Enterprises cryogenic rock magnetometer at the IRM. Weak magnetizations were also observed in previous studies of GRF tuffs (Tsukui and Clyde, 2012). GRF sediments had comparable NRM values to tuffs.

NRM intensity varies by stratigraphic position, as seen in Figure 2. NRM is relatively even from the bottom of the Tipton up through the lower Wilkins Peak Member before weakening around alluvial marker bed D. Intensity varies widely between the F and H alluvial marker beds due to the varied lithologies of the samples in that section. NRM then slowly increases into the Laney Member. These minor trends by stratigraphic position are overshadowed by variation of sample NRMs within each stratigraphic horizon. Figure 2 also shows average bulk susceptibility and the NRM/X ratio, which reflect similarly wide value ranges between samples that are close stratigraphically. Our interpretation of these parameters will be discussed below.

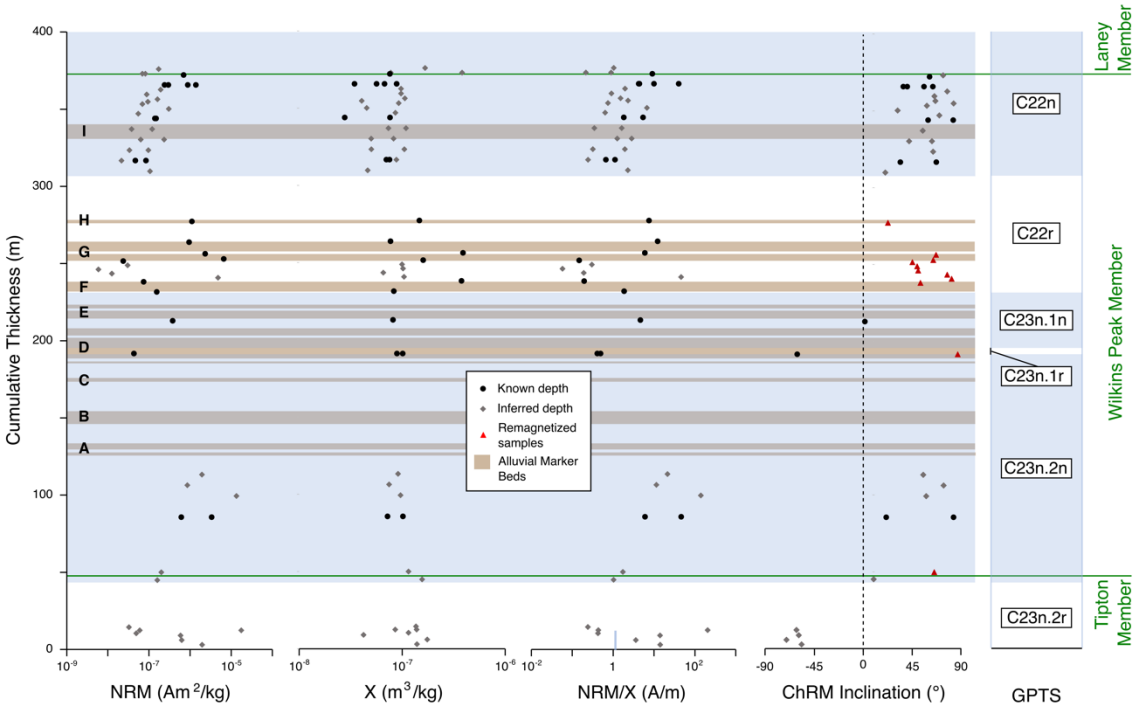

Figure 2. NRM, susceptibility, and NRM normalized by susceptibility (all shown at log scale), and inclination of samples by stratigraphic position. Cumulative thickness is derived from BF1: ERDA-LERC Blacks Fork 1 (Smith et al., 2010). Samples represented by black dots are tied to specific stratigraphic markers in BF1, while the position of samples represented by gray diamonds are at interpolated depths. Chron positions (pale blue overlay) within the stratigraphy are determined by the most recent GPTS (Ogg, 2020) overlain on the Bayesian model (Fig. 7) and adjusted by data from this study (Fig. 7). Remagnetized samples are represented by red triangles and are not used to determine chron positions.

Paleodirectional analysis of tuffs

Generally, orthogonal vector endpoint diagrams showed similar trends during both thermal and AF demagnetization (Fig. 3). Both demagnetization methods were able to reveal tuffs with normal and reversed polarities.

AF demagnetization of most tuff specimens in this study reached the origin after a 170 mT demagnetization step and showed only one clear magnetic component. In several

cases, remanence remained after the 170 mT step, indicating the presence of higher coercivity minerals. Most tuffs lost ~50% of their NRM intensity between 15-70 mT and lost ~100% between 50-170 mT. Some specimens revealed low coercivity secondary magnetizations that were usually removed after the 25 mT demagnetization step.

Thermal demagnetization of tuffs revealed a ~50% decrease in NRM intensity by 150-400°C and were fully demagnetized by 400-600°C. In some instances these materials were susceptible to mineralogic alteration during thermal demagnetization. New mineral growth was detected starting at ~400°C and identified using changes in bulk susceptibility after each thermal step as well as by identifying sudden increases in magnetization during thermal demagnetization. Measurements associated with experimentally induced mineral alteration were not used in determining ChRM directions. Secondary magnetizations were removed by 150°C.

Nearly all secondary magnetizations observed during AF and thermal demagnetization were of normal polarity with inclinations between 30-65° and likely reflect the viscous recording of the Earth's present-day field. Samples collected near topographic highpoints also displayed secondary magnetizations consistent with lightning strikes and were excluded from further analyses.

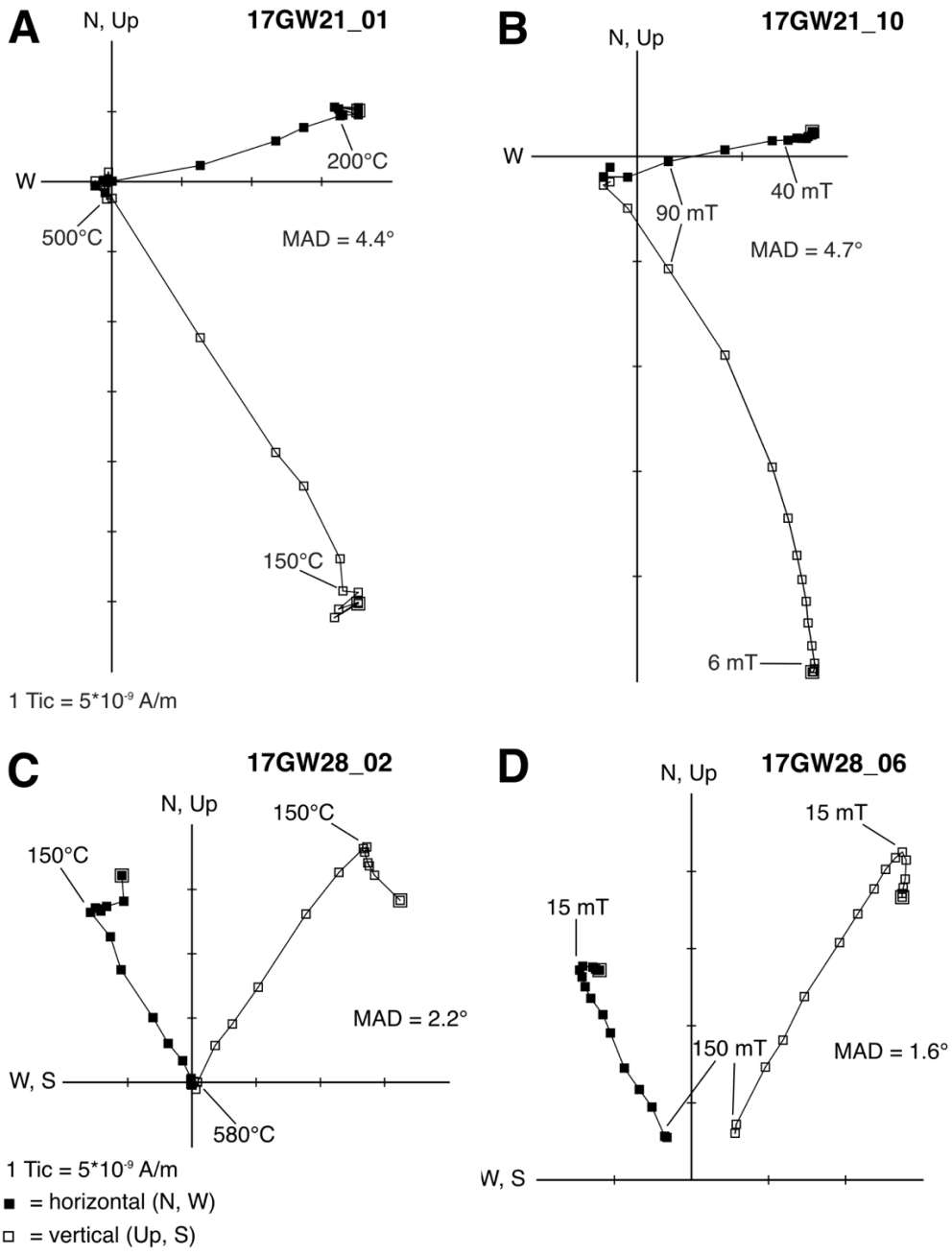

Figure 3. Vector end-point diagrams of a normal polarity site 17GW21 (A, B) and a reversed polarity site 17GW28 (C, D) demagnetized using thermal (A, C) and alternating-field (B, D) methods. Sample 17GW28 shows evidence of a normal overprint. Samples subjected to AF demagnetization do not fully reach the origin and therefore retain some magnetization after the 170 mT step.

Paleodirectional analysis of GRF sediments

ChRMs were resolved as discussed above, although most GRF sediments retained normal polarities and only one non-tuff sample was reversed (19GR1B). Normal ChRMs were generally indistinguishable from the modern field direction.

AF demagnetization of the GRF sediments in this study generally displayed one of two behaviors. In the first case, specimens showed one clear magnetic component that neatly trended towards the origin and lost most of its remanence by 50-100 mT. In some instances, the presence of higher coercivity materials was indicated as some remanence remained after the 170 mT step. In the second case, specimens were unusually weak and displayed one difficult to resolve magnetic component without a clear trend that was partially or totally obscured by noise.

Thermal demagnetization of GRF sediments indicated that the majority of remanence was lost by 300-400°C in most samples. Some specimens contained a second magnetic component that retained information up to ~650°C, although the direction preserved was usually similar to the direction of the first component. As above, some specimens displayed new mineral growth after ~400°C and measurements associated with this experimentally induced mineral alteration were not used in determining ChRM directions.

Statistics

Specimens were sorted by criteria to ensure results were robust for paleomagnetic analysis (Table 2). Out of a total of 565 total demagnetized specimens, the results of 70 were discarded due to equipment malfunctions. Results from 73 further specimens were rejected as they were obfuscated by noise, limiting reliable determination of ChRMs. 422 specimens were subjected to further analysis. Specimens with MAD values greater than 20° resulted in the rejection of 24 additional specimens. The remaining 398 specimens had an average MAD angle of 9.0° and were used to determine site mean directions for

44 total samples. 33 samples (300 specimens) of these record original paleomagnetic directions while 11 samples (98 specimens) contain directional data consistent with remagnetization due to alteration. Specimens were analyzed by their k and α95 parameters, in which a high k and a low α95 indicates better agreement between specimens within a site. Sites with lower parameters are characterized by more ChRM directional scatter but were internally consistent between specimens and polarity is reliably determined. Higher k values do not correlate with lower average MAD values. Similarly, the number of specimens used to determine k does not correlate with k value. The samples collected at the Gookin-White Mountain Road study area include both normal and reversed polarities. This set of samples passed an adapted inclination-only reversal test (after McFadden and Reid, 1982; McFadden and McElhinny, 1990) in which normal and reversed ChRM inclinations of specimens were presented as Cumulative Distribution Functions (CDF). Figure 4 shows that the distribution of normal and reversed inclinations is virtually indistinguishable at 1σ from the median. This style of reversal test was necessary given that many samples are azimuthally unoriented.

TABLE 2: PALEOMAGNETIC SAMPLES SORTED

Group Description	# Samples	# Specimens
Collected	70	-
Demagnetized	59	565
Removed results altered by equipment issues	52	495
Removed results obscured by noise	47	422
Removed specimens where MAD > 20°	44	398
Direction preserved determined to be original	33	300
Direction preserved determined to be altered	11	98

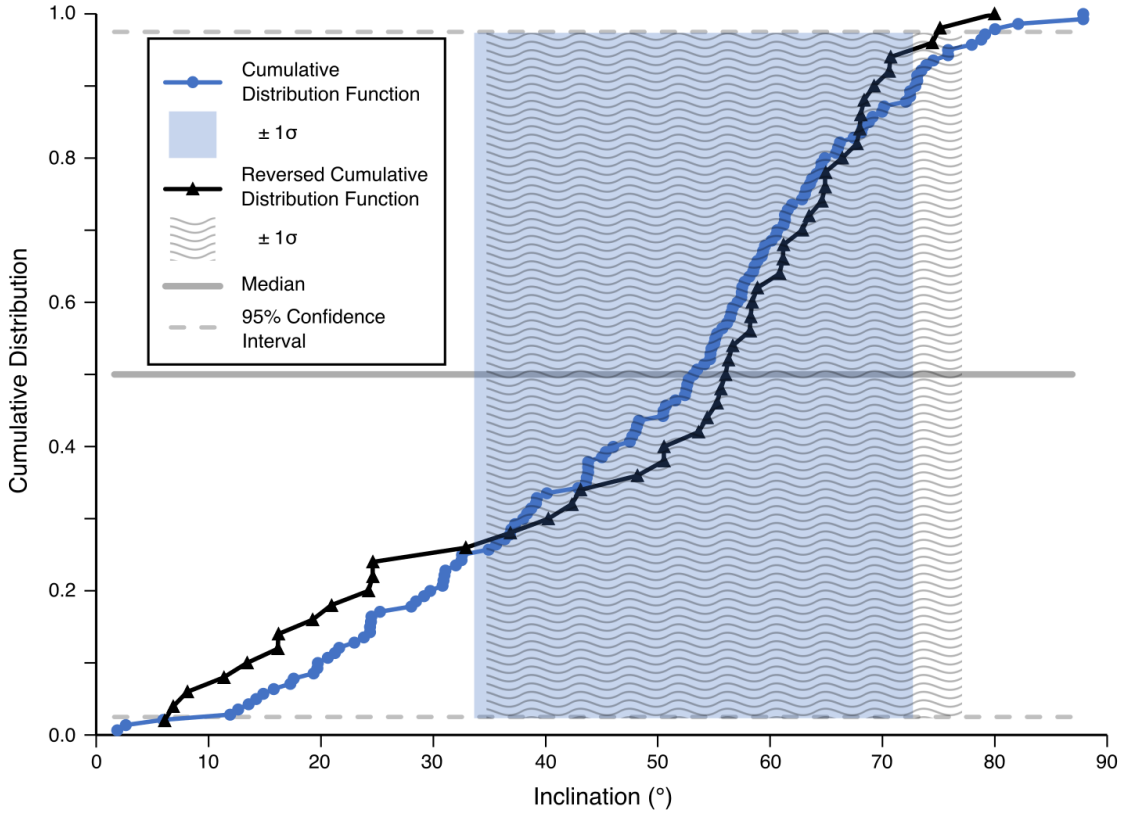

Figure 4. Adapted Cumulative Distribution Function (CDF) inclination-only reversals test using the ChRM of normal and reversed specimens from a stratigraphic section at Gookin-White Mountain Road (GW). The line with blue circles (black triangles) shows the cumulative distribution of specimens of normal (reversed) inclination. Normal and reversed CDF's are analogous and indicate passage of the reversals test, as demonstrated by the similarity of the functions 1σ from the median.

Magnetostratigraphic model

The polarity of each sample was determined for all samples that passed the quality criteria described above. Figure 2 shows polarity determinations for each tested sample by stratigraphic position, and Figure 5 shows all the polarity results for each tuff in relative position. The average inclination is 55.5° for sites with normal polarity and -61.6°

for reversed sites, which is statistically similar to the expected direction of 349°/61° for Eocene samples from southwestern Wyoming (Diehl et al., 1983). When similar ashfall tufts were analyzed, polarity results confirmed earlier work by Tsukui & Clyde (2012) in all but two cases. The Firehole tuff was identified as reversed by Tsukui & Clyde (2012), but is found here to be normally magnetized with data from two separate samples. The Rife tuff was identified as normal, but a tuff equivalent to the Rife was found here to be transitional. A large number of new sites were established within the stratigraphy, including the Analcite, Second, and Schegg's tuffs (or Schegg's tuff equivalent). Normally magnetized strata include all tuffs tested from the Church Butte to the Firehole tuffs. Five separate tuffs starting from below the Rife through the K-spar tuff were determined to have reversed polarity (Figure 5). A marly orange sample with high levels of Uranium and Thorium in the bottom third of the D-bed was determined to be reversed and is interpreted here to represent the subchron C23n.1r, although polarity was determined from only 4 specimens (see below). Directional data was unrecoverable from most non-tuff lithologies, leaving gaps in several crucial portions of the sediment assemblage assumed to be reversed.

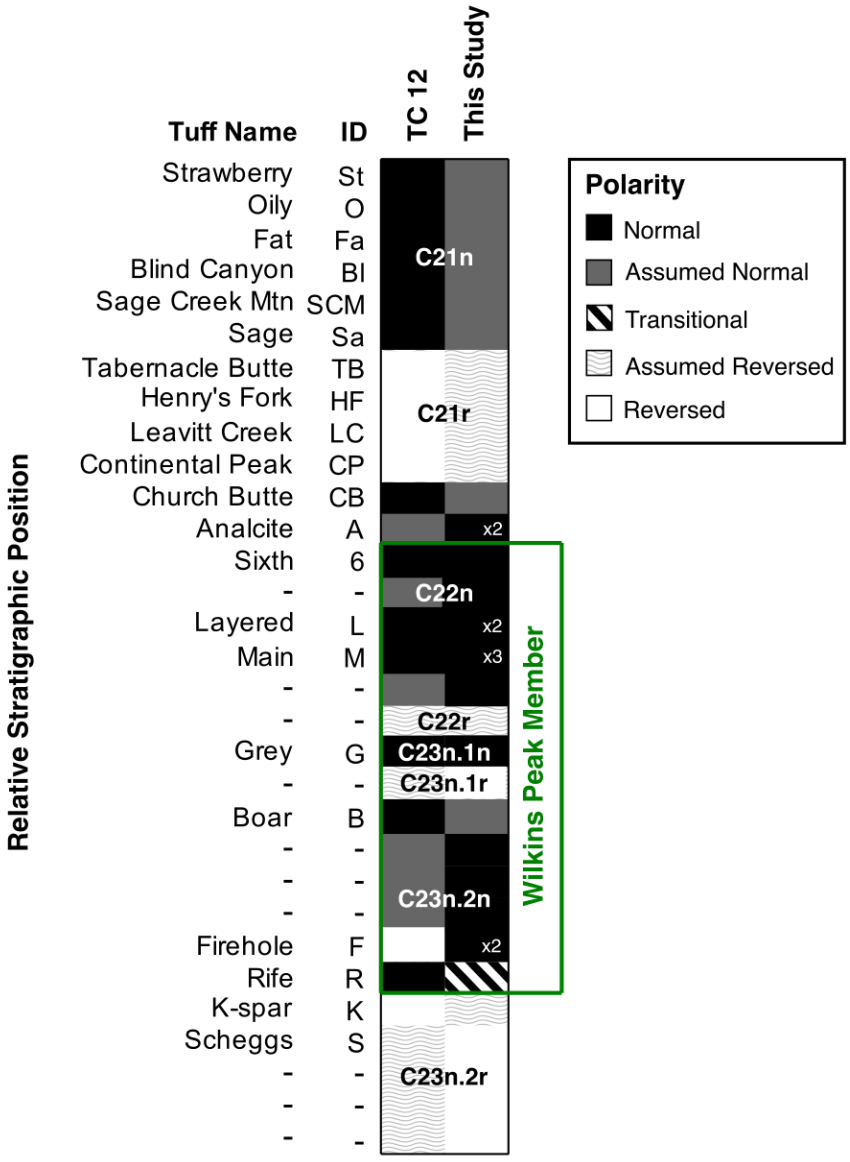

Figure 5. Polarity results for each sample. Tuffs are identified on the left and listed in order of their stratigraphic position. Columns indicate different paleomagnetic sampling campaigns for Green River Formation tuffs, including data from TC 12 = Tsukui and Clyde (2012). White (black) blocks indicate the corresponding tuff was reversed (normal) in that campaign, while light patterned (dark) shades of grey indicate inferred reversed (normal) polarity.

TABLE 3: MAGNETIC MINERALOGY

Site	Name	Abbrev.	NRM (Am^2/kg)	Tc (°C)	Ms (Am^2/kg)	Mr (Am^2/kg)	Bc (mT)	Bcr (mT)
16TR1	Sixth tuff	6	1.40×10^{-6}	535	6.33×10^{-4}	3.50×10^{-4}	37.7	48.1
16TR2	-	-	9.43×10^{-8}	534	2.68×10^{-4}	1.21×10^{-5}	14.3	43.6
16TR3	Layered tuff	L	1.50×10^{-7}	557 (650)	2.35×10^{-5}	6.86×10^{-6}	13.5	50.0
16TR4	-	-	1.20×10^{-7}	545 (660)	3.61×10^{-4}	9.50×10^{-6}	2.7	37.0
16TR5	-	-	6.33×10^{-8}	530	2.20×10^{-5}	8.40×10^{-6}	42.0	68.5
16TR6	-	-	9.71×10^{-8}	562	2.33×10^{-4}	1.64×10^{-5}	8.6	62.7
16TR7	Main tuff	M	4.71×10^{-8}	552 (659)	1.38×10^{-5}	2.40×10^{-6}	4.4	-
17GW01	Sixth Tuff	6	8.87×10^{-7}	569 (677)	7.93×10^{-4}	1.41×10^{-4}	28.7	40.8
17GW02	Sixth Tuff	6	2.98×10^{-7}	559	5.28×10^{-5}	7.79×10^{-6}	37.9	-65.0
17GW03	-	-	6.99×10^{-7}	550	6.96×10^{-4}	1.26×10^{-4}	19.6	-
17GW04	Sixth Tuff	6	2.40×10^{-7}	566	1.32×10^{-4}	2.45×10^{-5}	29.9	50.0
17GW05	-	-	1.92×10^{-7}	550	3.73×10^{-4}	3.80×10^{-5}	22.1	26.0
17GW06	-	-	8.87×10^{-8}	561	1.92×10^{-4}	4.71×10^{-5}	38.1	-
17GW07	-	-	1.62×10^{-7}	565	1.26×10^{-3}	1.46×10^{-4}	17.7	59.1
17GW08	-	-	6.92×10^{-8}	544	6.44×10^{-4}	3.02×10^{-5}	6.4	26.4
17GW09	-	-	3.04×10^{-7}	551	3.98×10^{-4}	2.86×10^{-5}	12.5	51.9
17GW10	-	-	5.49×10^{-8}	522	6.43×10^{-5}	3.75×10^{-6}	16.4	-
17GW11	Layered tuff	L	1.40×10^{-7}	575	5.82×10^{-4}	3.88×10^{-5}	10.8	-50.0
17GW13	-	-	2.34×10^{-7}	554	1.70×10^{-3}	6.35×10^{-5}	3.8	32.7
17GW16	- (one below main tuff)	-	1.06×10^{-7}	565	3.99×10^{-4}	2.45×10^{-5}	8.1	45.4
17GW21	Below Second = 22	-	1.96×10^{-6}	570	3.54×10^{-4}	9.68×10^{-5}	36.2	83.6
17GW22	Below Second = 21	-	1.35×10^{-5}	561	3.85×10^{-3}	1.86×10^{-3}	60.4	83.9
17GW23	Firehole	F	6.18×10^{-7}	546 (648)	7.33×10^{-4}	7.52×10^{-5}	16.7	88.5
17GW25	Schegg's Candidate	S	1.76×10^{-5}	557	2.79×10^{-3}	1.17×10^{-3}	29.3	40.6
17GW26	-	-	5.91×10^{-7}	553	6.20×10^{-4}	1.58×10^{-4}	20.1	55.8
17GW27	-	-	6.30×10^{-7}	549	8.35×10^{-3}	3.68×10^{-4}	2.6	16.3
17GW28	-	-	1.97×10^{-6}	541 (672)	1.67×10^{-3}	3.63×10^{-4}	14.5	34.9
19GR1A	Orange U-rich marker bed	-	4.21×10^{-8}	544	3.37×10^{-4}	1.28×10^{-5}	8.1	22.0
19GR1B	Orange U-rich marker bed	-	4.37×10^{-8}	539	2.75×10^{-4}	2.42×10^{-6}	0.5	60.0
19GR2*	5' Above Tipton	-	2.00×10^{-7}	561 (504)	6.35×10^{-4}	1.62×10^{-5}	5.4	39.4
19GR3	Firehole Tuff	F	3.37×10^{-6}	550	3.09×10^{-4}	2.36×10^{-4}	70.0	60.8
19GR4	Main Tuff	M	8.49×10^{-8}	565	-	-	-	-
19GR5	Above F, Below 2	-	8.59×10^{-7}	573	3.66×10^{-4}	2.47×10^{-5}	7.8	44.2
19GR6	Grey Tuff	G	3.80×10^{-7}	565	1.22×10^{-4}	1.47×10^{-5}	27.5	-
20AL03	Rife Equivalent	R	1.60×10^{-7}	547	6.56×10^{-5}	1.34×10^{-6}	4.1	-
20MM01	Analcite Tuff	A	6.94×10^{-8}	583	6.04×10^{-6}	4.82×10^{-6}	65.6	50.0
20FC02	Above F-bed	-	7.46×10^{-8}	572 (318)	7.61×10^{-2}	5.51×10^{-3}	8.5	56.3
20FC03	Above 02	-	4.80×10^{-6}	535	1.36×10^{-4}	8.34×10^{-6}	9.2	-
20FC04	Above 03	-	1.26×10^{-8}	587	2.37×10^{-5}	4.28×10^{-7}	4.3	-
20FC05	Above 04	-	5.89×10^{-9}	581	6.78×10^{-5}	2.47×10^{-6}	5.5	46.3
20FC06	Above 05	-	3.03×10^{-8}	566	1.93×10^{-6}	9.57×10^{-8}	10.8	-
20FC07	Lower G-bed	-	2.39×10^{-8}	570	7.64×10^{-3}	7.70×10^{-4}	11.8	60.6
20FC08	Middle G-bed	-	2.35×10^{-6}	572 (314)	2.13×10^{-2}	1.80×10^{-3}	8.7	50.1
20FC09	Larger beds w/in G-bed	-	6.63×10^{-6}	560	7.06×10^{-4}	3.50×10^{-5}	5.5	53.3
20FC11	H-bed	-	1.12×10^{-6}	549 (287)	1.75×10^{-3}	2.11×10^{-4}	10.0	55.8

Tc Primary (Secondary shown in parenthesis) Curie Temperature as determined by low field magnetic susceptibility tests in air
Ms Saturation Magnetization
Mr Saturation Remanence
Bc Coercivity
Hcr Coercivity of remanence

Magnetic Mineralogy

Magnetization and susceptibility data are summarized in Table 3.

Low field magnetic susceptibility measured as a function of temperature shows inflections consistent with one or two magnetic mineral phases in most specimens (Figure 6). Magnetite was found to be the primary magnetic mineral in most samples with small amounts of hematite also present in the majority of samples. The average Curie temperature (T_C) for magnetite in tuffs was 555°C with a range of 522 - 583°C, indicating that partial oxidation or titanium substitution has lowered the T_C from that of pure stoichiometric magnetite. Values for non-tuff lithologies were comparable, with an average of 559°C and a range of 532 - 587°C. Higher T_C ranging from 648-677°C, shown in parenthesis in Table 3, indicate the presence of metastable maghemite, or more probable hematite in some samples. The magnetic susceptibility data indicates that hematite is present in many other samples, but was not sufficient to quantitatively determine the T_C. Cooling curves generally showed slightly lower T_C values and often displayed a large jump in susceptibility associated with magnetite, indicating mineral alteration and growth at high temperatures. Pyrrhotite was a concern as it has been previously observed in GRF rocks (Sheriff and Shive, 1982), but a lack of T_C's at 320°C suggests that pyrrhotite was absent from our tuff samples or only present in minute quantities. Non-tuff samples, however, show ample evidence of pyrrhotite as indicated by secondary T_C's of 287 - 318°C. The presence of high-coercivity hematite and pyrrhotite in limited samples emphasizes the need for using thermal demagnetization in addition to the AF demagnetization method.

Demagnetization data is also useful for interpreting the magnetic mineralogy of GRF tuffs and sediments. In most tuff samples, the majority of remanence is thermally unblocked below the T_C of magnetite, confirming its role as the primary magnetic mineral carrier. In contrast, the majority of remanence in non-tuff lithologies is lost by around 300 - 400°C.

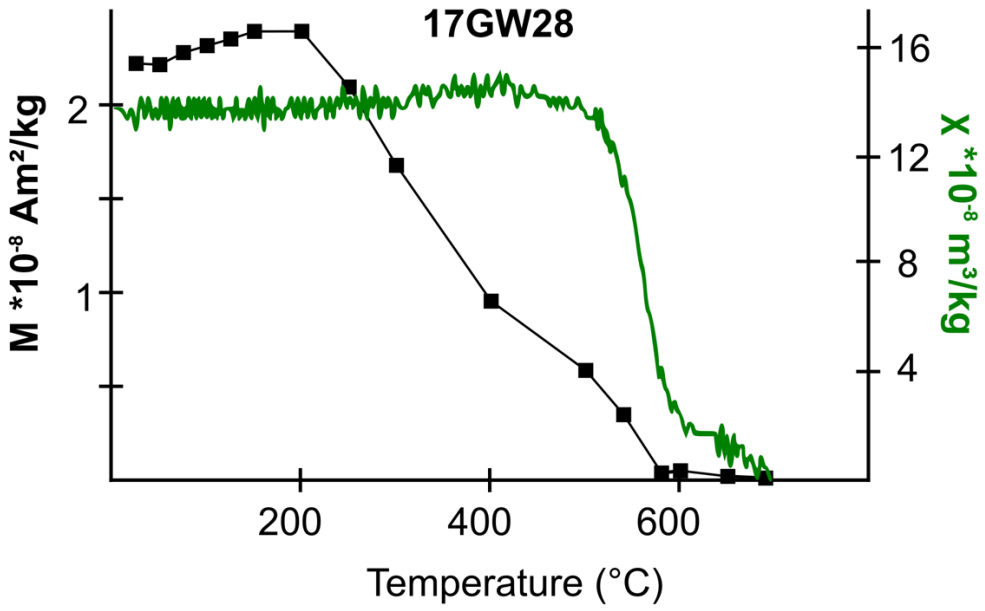

Figure 6. Example of typical low field-magnetic susceptibility (green undulating line) and magnetization (black line with squares) as a function of temperature for sample 17GW28.

Vibrating sample magnetometry

Major hysteresis loops and backfield curves provide information about the distribution of magnetic domain states within the GRF tuffs. Standard bulk values of Ms, Mr, Bc, and Bcr are shown in Figure 7 and in Table 3. Most hysteresis data fall within the 'pseudosingle domain' or vortex state region of a traditional Day plot (Day et al., 1977), and generally follows the trend of magnetic mixing lines defined by Dunlop (2002). The presence of hematite in some specimens causes elevated Mr/Ms and Bc/Bcr values in some instances, leading to an offset from the magnetite mixing lines of Dunlop (2022). On a squareness-coercivity plot (Fig. 6B), a linear regression for unheated GRF tuff specimens is broadly consistent with the pure magnetite trend defined by Wang and Van der Voo (2004). Interestingly, a linear regression for tuff samples after thermal demagnetization shows a different trend where coercivity increases more rapidly than Mr/Ms ratios, which would be consistent with the formation of nanoscale hematite during repeated thermal cycling.

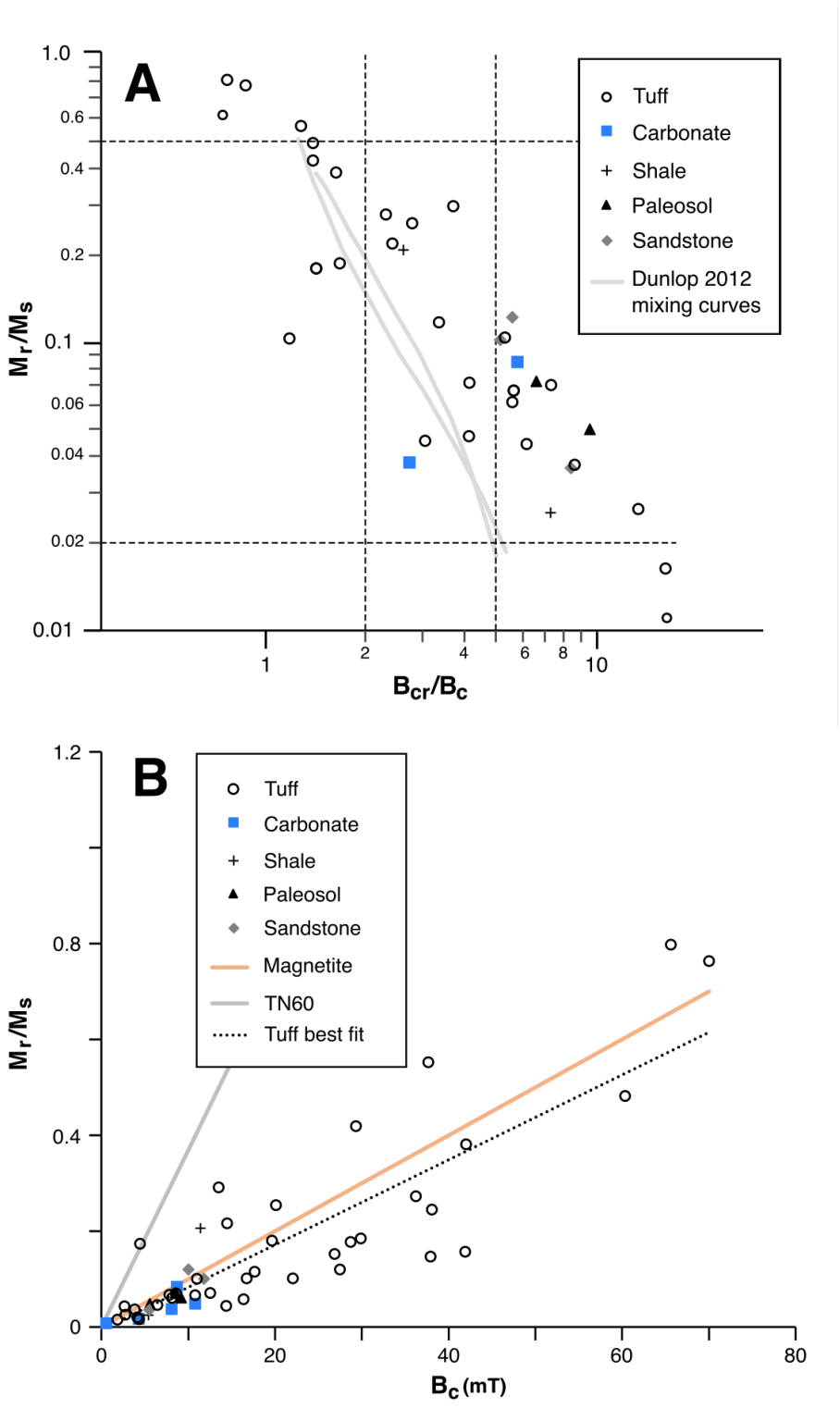

Figure 7. Hysteresis data from samples in this study plotted by lithology in a Day plot (1977) (A) and a squareness plot with fit lines from Wang & Van der Voo plot (2004) (B).

DISCUSSION

Paleomagnetic reliability of ash fall tuffs in the GRF

Magnetic mineralogy and demagnetization results indicate that tuff samples are generally reliable paleomagnetic recorders. Magnetite or its cation-substituted variants are the dominant remanence carriers and record ChRM directions. Ash-fall tuffs deposited in a lacustrine environment acquired DRMs, and there is little evidence of post-depositional minerals holding remanence, such as goethite or pyrrhotite, which are known to affect most other Green River Formation lithologies (see below). The declination and inclination data of fully oriented tuff samples are consistent with expected directions for the Eocene. Poorly-defined or unreliable sites were identified and removed from further analyses. Although some samples may have experienced minor post-depositional mineral growth, chemical alteration, or small rotation or slump of beds, these factors are not significant enough to negatively impact our ability to determine magnetic polarity. Therefore, the tuff samples are considered generally reliable as geomagnetic recorders.

Paleomagnetic problems associated with non-tuff GRF sediments

Non-tuff lithologies in the GRF tend to be poor paleomagnetic recorders as originally described by Sheriff and Shive (1982). As a case study to explore whether modern paleomagnetic protocols could resolve ChRMs from non-tuff lithologies, we collected oriented samples of every competent unit in an exposed section within Firehole Canyon. This section was particularly important in our efforts to identify evidence of chron C22r within the Wilkins Peak Member, and coincides with a portion of the stratigraphy that is generally devoid of tuffs (Fig. 7). The exposed sediments in this section included paleosols, organic-poor shales, fine-grained sandstones, and limestones and are generally representative of Wilkins Peak member lithologies. Whenever possible strata thicker than 2 cm were sampled, though much of the Wilkins Peak member consists of finely laminated, friable, and loose sediments in outcrop exposures, limiting

paleomagnetic sampling. Although these sediments had magnetizations that were as weak as the ashfall tufts, their ChRM directions were indistinguishable from that of the modern field and the majority of remanence was lost by 300°C, indicating that magnetization was likely held by secondary sulfides, such as pyrrhotite. Low-field susceptibility tests indicated pyrrhotite as a magnetic mineral. The residual magnetization after the 300°C demagnetization step for these samples was also consistent with the modern field direction and was stable up to temperatures of ~650°C, indicating secondary hematite as a likely magnetic carrier. These sediment samples also displayed large increases in low field susceptibility after thermal demagnetization steps >400°C, suggesting that the magnetic mineralogy was altering during heating. These findings are consistent with sedimentological interpretations reporting multiple generations of secondary and even tertiary alteration of GRF sediments in the form of shortite, pyrite, pyrrhotite, goethite, and marcasite (Tuttle and Goldhaber, 1993; Jagniecki et al., 2013). Thus, Wilkins Peak member sediments were not reliable paleomagnetic recorders as they are impacted by multiple episodes of secondary magnetic mineral growth, they record the modern field, and tend to alter during thermal demagnetization.

One non-tuff sample, 19GR1, is of particular interest to this study due its more optimal paleomagnetic recording behavior and important position within the stratigraphy. Two small samples 19GR1A and 19GR1B were collected meters apart from the same marly orange bed in the lower third of the D-bed. This orange bed is known to be enriched in uranium and thorium, leading to its use as a marker bed in gamma-ray logs of the GRF and allowing for confident placement within the WPM stratigraphy (Michael +Smith, private correspondence). 19GR1A yielded a direction of 312.5°/86.9°, and is interpreted as being overprinted by the modern field. The ChRM for 19GR1A was constrained by AF data collected between the 30 and 110 mT steps and thermal demagnetization only up to 250°C. By contrast, 19GR1B displays a reversed direction that could record the short subchron C23n.1r, anchoring a key section of the magnetostratigraphy of the GRF (Fig. 2, 7). Remanence was lost by 300-400°C and 15-25 mT, but low field magnetic susceptibility of the sample indicates magnetite as a primary magnetic mineral.

Specimens from 19GR1B display high internal consistency with k = 132.7. Both samples were very weak with NRMs on the order of 10^{-8} Am^2kg^{-1}.

This interpretation of subchron C23n.1r should be tempered with caution. Only 4 specimens were subjected to demagnetization due to the small sample size. In this study, we construct a Wilkins Peak member magnetostratigraphy using 19GR1B as a reversed sample, but we urge caution.

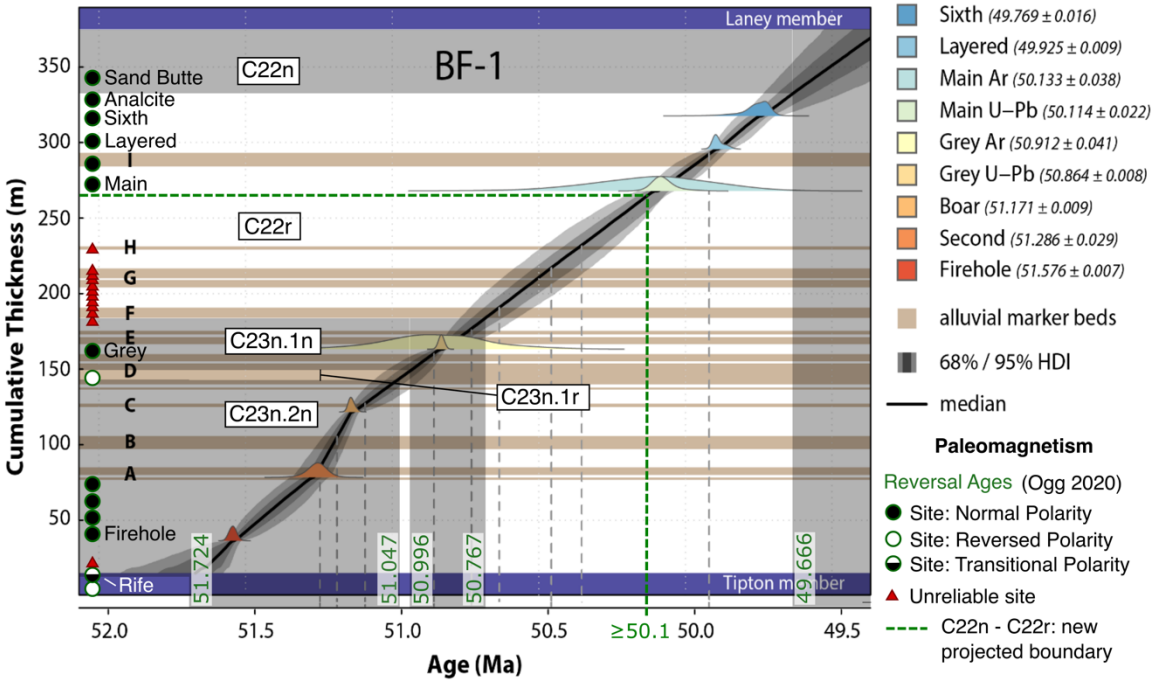

Figure 8. Bayesian age-depth model for the Wilkins Peak Member (WPM) of the Green River Formation for the ERDA-LERC Blacks Fork 1 Core. Black line indicates the median of the summed probability distribution shown in gray. Dashed gray lines project the top of each marker bed to a modeled age. Gray transparent overlays indicate normal polarity chrons with reversal ages from Ogg (2020) and their approximate stratigraphic position. Normal (reversed) polarity tuffs from this study are shown in stratigraphic position as circles filled with black (white). Triangles indicate the position of samples that did not yield reliable results. The dense green dashed line approximates the new proposed position of the C22n - C22r boundary which has a minimum age of 50.1 Ma derived from the main tuff. Adapted from Bruck (2020).

An updated magnetostratigraphy for the Wilkins Peak Member

The distribution of tuffs with the GRF is not uniform and varies in density by stratigraphic position. As mentioned above, certain key sections contain few or no tuffs, limiting sampling and making magnetostratigraphic interpretations challenging. To address these limitations, we leverage the Bayesian age model developed by Bruck & Singer (Bruck et al., 2020) to create an updated magnetostratigraphy for the Wilkins Peak Member (WPM) of the Green River Formation. Radioisotopic dates on tuffs from Bruck & Singer (Bruck et al., 2020) provide ages to the stratigraphy and assume linear sedimentation rates between dated tuffs. The Bayesian age model improves on previous data due to a greater density of sampled sites and decreased uncertainty of ages using modern $^{40}Ar/^{39}Ar$ and U–Pb techniques. The Geomagnetic Polarity Time Scale (Ogg, 2020) was projected onto the stratigraphy using the Bayesian age model and compared to our magnetic polarity findings thereby allowing several interpretations. This study confirms the position and age of the C23n.2n - C23r boundary at 51.7 Ma by identifying a Rife-equivalent tuff 2m below the Tipton - Wilkins Peak Boundary that records a transitional polarity. Previous work indicates that the Rife tuff is normally magnetized (Tsukui and Clyde, 2012), indicating the tuffs may not be a perfect correlation. Our study suggests a new age of ≥ 50.1 Ma for the C22n - C22r reversal using the Main Tuff as a minimum age, which is older than the astronomically tuned age of 49.666 Ma reported in Ogg (2020). Indeed, the difference in age for this reversal between the astronomically tuned record of Ogg (2020) and our own radioisotopically constrained model is roughly one long eccentricity cycle (~400 ka). Although a heroic effort was made to use non-tuff lithologies in Firehole Canyon to constrain the ages of the C22n-C22r and C22r-C23n.1n reversals (see above), none of these sediments provided reliable ChRM directions. Thus, we report a lack of reversed polarity samples representing C22r. Additionally, while we tentatively identified the short reversed subchron C23n.1r, more sampling is needed to test this interpretation. Ongoing work will address variable sedimentation rates and integrate the magnetostratigraphy and Bayesian models with cyclostratigraphy age models.

Our updated magnetostratigraphy refines the time scale of the GRF and helps unite marine and terrestrial records of the Eocene. This study expands on the work of Tsukui & Clyde (2012) by adding 60 samples (560 specimens) to 19 existing samples (120 specimens) with a particular focus on the WPM (Fig. 5). Well-constrained new radioisotopic dates from Bruck (2020) combined with paleomagnetic data greatly refine the magnetostratigraphic time scale, as seen in Figure 9. The comparison of marine and terrestrial age models for the Eocene in the figure demonstrates the correlations that will help paint a complete picture of the Early Eocene and the EECO. Understanding the changing climate of the EECO requires the comparison of data from varied sources using precise age models to determine the pace of significant events or climate signals, as in Hyland et al. (2017). GRF magnetostratigraphy can link these sources for future interdisciplinary climate studies of the EECO.

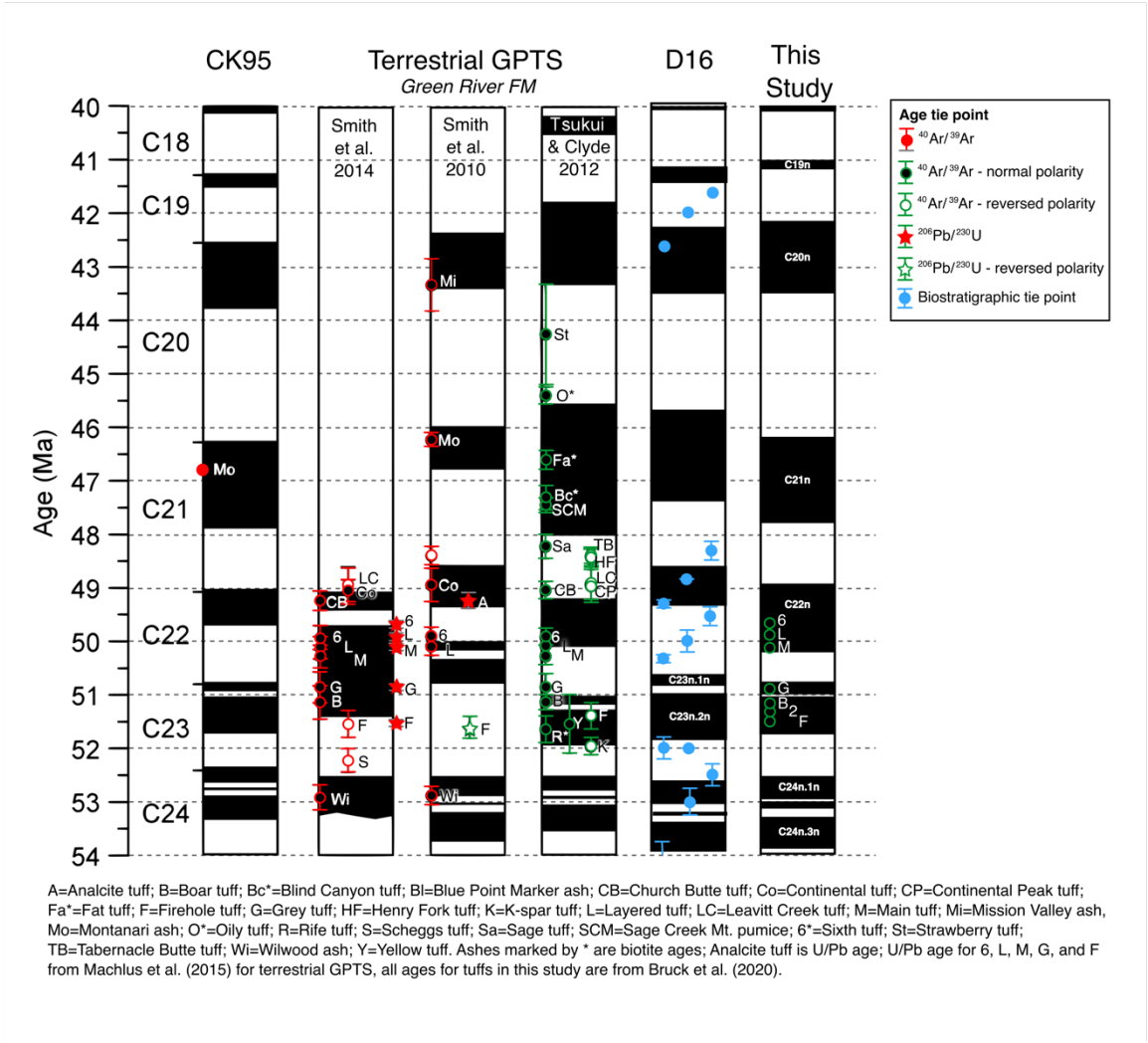

Figure 9. Comparison of Eocene geomagnetic polarity time scale models between CK95 (Cande and Kent, 1995), previous work on the GRF (Smith et al., 2010, 2014; Tsukui and Clyde, 2012), D16 (Dallanave et al., 2016), and this study. Circles (stars) with error bars serve as calibration points and represent $^{40}Ar/^{39}Ar$ ($^{206}Pb/^{230}U$) ages with a fill color of black (white) indicating normal (reversed) polarity in all but D15, where blue circles in D16 indicate biostratigraphic tie points. Chron boundaries are tied to calibration points and the most recent GPTS when the data was published (e.g. Ogg, 2020). The figure compares the differences between models, including adjustments to chron boundaries and tie point positions. A key highlight is the advancement of dating techniques (error bars for this study are smaller than the plot symbols) and the need to integrate marine and terrestrial records to form the most complete Eocene time scale. Figure adapted from Westerhold (2017).

Future Research

Ultimately, it may not be possible to acquire evidence of all subchrons known to occur during the deposition of the Wilkins Peak Member. It may be feasible to conduct additional sampling of tuffs in the northern portion of the GRF basin, which is closer to the source of volcanic material and may help refine some of the reversal ages. However, this same portion of the basin is more condensed in its sedimentation history than the depocenter that is the focus of this study. Efforts to incorporate paleomagnetic results from nearby basins or adjacent paleosols have the potential to help further refine the magnetostratigraphy of the Wilkins Peak Member (Smith et al., 2008; Hyland et al., 2017), but such correlations must be made with caution due to inherent stratigraphic ambiguities. Drill cores provide another attractive record, but can prove difficult to access, or may consist of a compressed section with less detail and limited quantities of material for destructive paleomagnetic or radioisotopic testing. Still, drill cores could present an avenue to test difficult-to-access segments of the stratigraphy or sediments exposed to more limited weathering, and often have the additional benefit of being well-documented (e.g. Walters et al., 2020).

CONCLUSIONS

This study establishes a robust magnetostratigraphy for the Wilkins Peak member of the Green River Formation. GRF ash-fall tuffs were well distributed within the section and confirmed to be reliable paleomagnetic recorders with little evidence of post-depositional alteration and were therefore the focus of this study. Non-tuff lithologies were tested in crucial tuff-poor sections of the stratigraphy, but displayed evidence of alteration and recorded directions close to the modern field and were therefore omitted from the magnetostratigraphy. Tuffs were sampled densely in the WPM, providing opportunities to refine the stratigraphic position of reversals. These new paleomagnetic data combined with recently published radioisotopic ages provide important updates to previously established chronology most importantly the determination of a new age of ≥50.1 Ma for the C22n - C22r reversal boundary in the Geomagnetic Polarity Time Scale. Additionally, the Firehole tuff was discovered to be normally magnetized, and an equivalent of the Rife tuff was determined to record transitional polarity placing the C23n.2n - C23r boundary ~2m below the Tipton - Wilkins Peak boundary. Additionally, the stratigraphic position of C23n.1r was tentatively identified, although more evidence is needed for a more conclusive interpretation. The updated GRF magnetostratigraphy presented here constrains the GRF time scale to aid studies of cyclostratigraphy and shifts in climate, refines the GPTS, and provides much-needed correlation between marine and terrestrial records of the Early Eocene Climatic Optimum.

BIBLIOGRAPHY

Aswasereelert, W., Meyers, S.R., Carroll, A.R., Peters, S.E., Smith, M.E., and Feigl, K.L., 2013, Basin-scale cyclostratigraphy of the Green River Formation, Wyoming: Geological Society of America Bulletin, v. 125, p. 216–228, doi:10.1130/B30541.1.

Bradley, W.H., 1964, Geology of Green River Formation and associated Eocene rocks in southwestern Wyoming and adjacent parts of Colorado and Utah: Professional Paper USGS Numbered Series 496-A, http://pubs.er.usgs.gov/publication/pp496A (accessed December 2019).

Bruck, B., Singer, B.S., Schmitz, M.D., and Jicha, B.R., 2020, A Bayesian age-depth model of the Wilkins Peak Member of the Eocene Green River Formation: v. 2020, p. V036- 07.

Cande, S.C., and Kent, D.V., 1995, Revised calibration of the geomagnetic polarity timescale for the Late Cretaceous and Cenozoic: Journal of Geophysical Research: Solid Earth, v. 100, p. 6093–6095, doi:10.1029/94JB03098.

Chamberlain, C.P., Wan, X., Graham, S.A., Carroll, A.R., Doebbert, A.C., Sageman, B.B., Blisniuk, P., Kent-Corson, M.L., Wang, Z., and Chengshan, W., 2013, Stable isotopic evidence for climate and basin evolution of the Late Cretaceous Songliao basin, China: Palaeogeography Palaeoclimatology Palaeoecology, v. 385, p. 106–124, doi:10.1016/j.palaeo.2012.03.020.

Chetel, L.M., Janecke, S.U., Carroll, A.R., Beard, B.L., Johnson, C.M., and Singer, B.S., 2011, Paleogeographic reconstruction of the Eocene Idaho River, North American Cordillera: GSA Bulletin, v. 123, p. 71–88, doi:10.1130/B30213.1.

Clyde, W.C., Sheldon, N.D., Koch, P.L., Gunnell, G.F., and Bartels, W.S., 2001, Linking the Wasatchian/Bridgerian boundary to the Cenozoic Global Climate Optimum: new magnetostratigraphic and isotopic results from South Pass, Wyoming: Palaeogeography, Palaeoclimatology, Palaeoecology, v. 167, p. 175–199, doi:https://doi.org/10.1016/S0031-0182(00)00238-8.

Clyde, W.C., Stamatakos, J., and Gingerich, P.D., 1994, Chronology of the Wasatchian land-mammal age (early Eocene); magnetostratigraphic results from the McCullough Peaks section, northern Bighorn Basin, Wyoming: Journal of Geology, v. 102, p. 367–377.

Clyde, W.C., Zonneveld, J.-P., Stamatakos, J., Gunnell, G.F., and Bartels, W.S., 1997, Magnetostratigraphy across the Wasatchian/Bridgerian NALMA boundary (early to middle Eocene) in the western Green River basin, Wyoming: Journal of Geology, v. 105, p. 657–669.

Culbertson, W.C., 1961, Stratigraphy of the Wilkins Peak member of the Green River Formation, Firehole Basin Quadrangle, Wyoming, Article 348: U. S. Geological Survey Professional Paper, p. D170–D173.

Dallanave, E., Bachtadse, V., Crouch, E.M., Tauxe, L., Shepherd, C.L., Morgans, H.E.G., Hollis, C.J., Hines, B.R., and Sugisaki, S., 2016, Constraining early to middle Eocene climate evolution of the Southwest Pacific and Southern Ocean: Earth and Planetary Science Letters, v. 433, p. 380–392, doi:http://dx.doi.org/10.1016/j.epsl.2015.11.010.

Day, R., Fuller, M., and Schmidt, V.A., 1977, Hysteresis properties of titanomagnetites: Grain-size and compositional dependence: Physics of the Earth and Planetary Interiors, v. 13, p. 260–267, doi:10.1016/0031-9201(77)90108-X.

Diehl, J.F., Beck, M.E., Beske-Diehl, S., Jacobson, D., and Hearn, B.C., 1983, Paleomagnetism of the Late Cretaceous-early Tertiary north-central Montana alkalic province: Journal of Geophysical Research, v. 88, p. 10593–10609, doi:http://dx.doi.org/10.1029/JB088iB12p10593.

Dunlop, D.J., 2002, Theory and application of the Day plot (Mrs/Ms versus Hcr/Hc) 2. Application to data for rocks, sediments, and soils: Journal of Geophysical Research: Solid Earth, v. 107, p. EPM 5-1-EPM 5-15, doi:https://doi.org/10.1029/2001JB000487.

Fenzan, R.J., 1978, A paleomagnetic study of a borehole core from the Mahogany Ledge member of the Green River formation [undergraduate thesis]: The Ohio State University, 10 p.

Frantz, C.M., Petryshyn, V.A., Marenco, P.J., Tripati, A., Berelson, W.M., and Corsetti, F.A., 2014, Dramatic local environmental change during the Early Eocene Climatic Optimum detected using high resolution chemical analyses of Green River Formation stromatolites: Palaeogeography, Palaeoclimatology, Palaeoecology, v. 405, p. 1–15, doi:10.1016/j.palaeo.2014.04.001.

Fugitt, D.S., 1976, Paleomagnetic study of oil shales from central Utah [undergraduate thesis]: The Ohio State University, 33 p.

Greenwood, D.R., and Wing, S.L., 1995, Eocene continental climates and latitudinal temperature gradients: Geology, v. 23, p. 1044–1048, doi:10.1130/0091-7613(1995)023<1044:ECCALT>2.3.CO;2.

Griggs, R.L., 1968, Altered tuffaceous rocks of the Green River Formation in the Piceance Creek Basin, Colorado: Open-File Report Report 68–113, doi:10.3133/ofr68113.

Hayashida, A., Kamata, H., and Danhara, T., 1996, Correlation of widespread tephra deposits based on paleomagnetic directions: Link between a volcanic field and sedimentary sequences in Japan: Quaternary International, v. 34–36, p. 89–98, doi:10.1016/1040-6182(95)00072-0.

Hyland, E.G., and Sheldon, N.D., 2013, Coupled CO2-climate response during the Early Eocene Climatic Optimum: Palaeogeography, Palaeoclimatology, Palaeoecology, v. 369, p. 125–135, doi:10.1016/j.palaeo.2012.10.011.

Hyland, E.G., Sheldon, N.D., and Cotton, J.M., 2017, Constraining the early Eocene climatic optimum: A terrestrial interhemispheric comparison: GSA Bulletin, v. 129, p. 244–252, doi:10.1130/B31493.1.

Ivany, L.C., Lohmann, K.C., Hasiuk, F., Blake, D.B., Glass, A., Aronson, R.B., and Moody, R.M., 2008, Eocene climate record of a high southern latitude continental shelf: Seymour Island, Antarctica: GSA Bulletin, v. 120, p. 659–678, doi:10.1130/B26269.1.

Iwaki, H., and Hayashida, A., 2003, Paleomagnetism of Pleistocene widespread tephra deposits and its implication for tectonic rotation in central Japan: Island Arc, v. 12, p. 46–60, doi:https://doi.org/10.1046/j.1440-1738.2003.00378.x.

Jagniecki, E.A., Jenkins, D.M., Lowenstein, T.K., and Carroll, A.R., 2013, Experimental study of shortite (Na2Ca2(CO3)3) formation and application to the burial history of the Wilkins Peak Member, Green River Basin, Wyoming, USA: Geochimica et Cosmochimica Acta, v. 115, p. 31–45, doi:10.1016/j.gca.2013.04.005.

Jagniecki, E., and Lowenstein, T., 2015, Evaporites of the Green River Formation, Bridger and Piceance Creek Basins: Deposition, Diagenesis, Paleobrine Chemistry, and Eocene Atmospheric CO2, in p. 277–312, doi:10.1007/978-94-017-9906-5_11.

Johnson, R.C., Mercier, T.J., Ryder, R.T., Brownfield, M.E., and Self, J.G., 2011, Assessment of in-place oil shale resources of the Eocene Green River Formation, greater Green River basin, Wyoming, Colorado, and Utah: U. S. Geological Survey Digital Data Series, p. 63.

Karoly, W.M., 1974, Paleomagnetic determinations of Green River oil shales of the Piceance Creek Basin, Colorado [undergraduate thesis]: The Ohio State University, 40 p.

Lauretano, V., Zachos, J.C., and Lourens, L.J., 2018, Orbitally Paced Carbon and Deep-Sea Temperature Changes at the PeaK of the Early Eocene Climatic Optimum: Paleoceanography and Paleoclimatology, v. 33, p. 1050–1065, doi:10.1029/2018PA003422.

Lowenstein, T.K., and Demicco, R.V., 2006, Elevated Eocene Atmospheric CO2 and Its Subsequent Decline: Science, v. 313, p. 1928–1928, doi:10.1126/science.1129555.

Lurcock, P.C., and Wilson, G.S., 2012, PuffinPlot: A versatile, user-friendly program for paleomagnetic analysis: Geochem. Geophys. Geosyst., v. 13, p. Q06Z45, doi:10.1029/2012GC004098.

McFadden, P.L., and McElhinny, M.W., 1990, Classification of the reversal test in palaeomagnetism: Geophysical Journal International, v. 103, p. 725–729, doi:10.1111/j.1365-246X.1990.tb05683.x.

McFadden, P.L., and Reid, A.B., 1982, Analysis of palaeomagnetic inclination data: Geophysical Journal International, v. 69, p. 307–319, doi:10.1111/j.1365-246X.1982.tb04950.x.

Murphey, P.C., 2001, Stratigraphy, fossil distribution, and depositional environments of the upper Bridger Formation (middle Eocene) of southwestern Wyoming, and the taphonomy of an unusual Bridger microfossil assemblage [Doctoral]: University of Colorado at Boulder, Boulder, CO, United States (USA), 346 p., http://search.proquest.com/georef/docview/51960678/citation/DB3C79EA52EE4496PQ/1 (accessed December 2019).

Ogg, J., 2020, Geomagnetic Polarity Time Scale, in p. 159–192, doi:10.1016/B978-0-12-824360-2.00005-X.

Pearson, P.N., Ditchfield, P.W., Singano, J., Harcourt-Brown, K.G., Nicholas, C.J., Olsson, R.K., Shackleton, N.J., and Hall, M.A., 2001, Warm tropical sea surface temperatures in the Late Cretaceous and Eocene epochs: Nature, v. 413, p. 481–487, doi:10.1038/35097000.

Pietras, J.T., and Carroll, A.R., 2006, High-Resolution Stratigraphy of an Underfilled Lake Basin: Wilkins Peak Member, Eocene Green River Formation, Wyoming, U.S.A.: Journal of Sedimentary Research, v. 76, p. 1197–1214, doi:10.2110/jsr.2006.096.

Ratterman, N.G., Surdam, R.C., Sheppard, R.A., and Mumpton, F.A., 1981, Zeolite mineral reactions in a tuff in the Laney Member of the Green River Formation, Wyoming: Clays and Clay Minerals, v. 29, p. 365–377.

Reynolds, R.L., 1979, Comparison of the TRM of the Yellowstone Group and the DRM of some Pearlette ash beds: Journal of Geophysical Research: Solid Earth, v. 84, p. 4525–4532, doi:https://doi.org/10.1029/JB084iB09p04525.

Richardson, K.G., 1980, Paleomagnetic study of the Mahogany oil shale, Uinta Basin, Utah [undergraduate thesis]: The Ohio State University, 124 p.

Roehler, H.W., 1992, Correlation, composition, areal distribution, and thickness of Eocene stratigraphic units, greater Green River basin, Wyoming, Utah, and Colorado: U. S. Geological Survey Professional Paper, p. E1–E49.

Sewall, J.O., and Sloan, L.C., 2006, Come a little bit closer: A high-resolution climate study of the early Paleogene Laramide foreland: Geology, v. 34, p. 81–84, doi:10.1130/G22177.1.

Sheriff, S.D., and Shive, P.N., 1982, Unreliable paleomagnetic results from the Wilkins Peak Member of the Eocene Green River Formation, Wyoming: Geophysical Research Letters, v. 9, p. 723–726, doi:http://dx.doi.org.ezp2.lib.umn.edu/10.1029/GL009i006p00723.

Smith, M.E., Carroll, A.R., Scott, J.J., and Singer, B.S., 2014, Early Eocene carbon isotope excursions and landscape destabilization at eccentricity minima: Green River Formation of Wyoming: Earth and Planetary Science Letters, v. 403, p. 393–406, doi:10.1016/j.epsl.2014.06.024.

Smith, M.E., Carroll, A.R., and Singer, B.S., 2008, Synoptic reconstruction of a major ancient lake system: Eocene Green River Formation, western United States: GSA Bulletin, v. 120, p. 54–84, doi:10.1130/B26073.1.

Smith, M.E., Chamberlain, K.R., Singer, B.S., and Carroll, A.R., 2010, Eocene clocks agree; coeval (super 40) Ar/ (super 39) Ar, U-Pb, and astronomical ages from the Green River Formation: Geology (Boulder), v. 38, p. 527–530, doi:http://dx.doi.org.ezp3.lib.umn.edu/10.1130/G30630.1.

Strangway, D.W., and McMahon, B.E., 1973, Paleomagnetism of Annually Banded Eocene Green River Sediments: Journal of Geophysical Research, v. 78, p. 5237–5245.

Sullivan, R., 1980, A stratigraphic evaluation of the Eocene rocks of southwestern Wyoming: Report of Investigations - Geological Survey of Wyoming, p. 50.

Tauxe, L., Gee, J., Gallet, Y., Pick, T., and Bown, T., 1994, Magnetostratigraphy of the Willwood Formation, Bighorn Basin, Wyoming; new constraints on the location of Paleocene/Eocene boundary: Earth and Planetary Science Letters, v. 125, p. 159–172.

Tsukui, K., and Clyde, W.C., 2012, Fine-tuning the calibration of the early to middle Eocene geomagnetic polarity time scale: Paleomagnetism of radioisotopically dated tuffs from Laramide foreland basins: GSA Bulletin, v. 124, p. 870–885, doi:10.1130/B30545.1.

Tuttle, M.L., and Goldhaber, M.B., 1993, Sedimentary sulfur geochemistry of the Paleogene Green River Formation, western USA: Implications for interpreting depositional and diagenetic processes in saline alkaline lakes: Geochimica et Cosmochimica Acta, v. 57, p. 3023–3039, doi:10.1016/0016-7037(93)90291-4.

Vandenberghe, N., Hilgen, F.J., Speijer, R.P., Gradstein, F.M., Ogg, J.G., Schmitz, M.D., and Ogg, G.M., 2012, The Paleogene Period: Elsevier, p. 855–921, doi:http://dx.doi.org.ezp3.lib.umn.edu/10.1016/B978-0-444-59425-9.00028-7.

Walters, A.P., Meyers, S.R., Carroll, A.R., Hill, T.R., and Vanden Berg, M.D., 2020, Lacustrine cyclicity in the early Eocene Green River Formation, Uinta Basin, Utah: Evidence from X-ray fluorescence core scanning: Journal of Sedimentary Research, v. 90, p. 429–447, doi:10.2110/jsr.2020.24.

Wang, D., and Van der Voo, R., 2004, The hysteresis properties of multidomain magnetite and titanomagnetite/titanomaghemite in mid-ocean ridge basalts: Earth and Planetary Science Letters, v. 220, p. 175–184, doi:10.1016/S0012-821X(04)00052-4.

Westerhold, T. et al., 2017, Astronomical calibration of the Ypresian timescale: implications for seafloor spreading rates and the chaotic behavior of the solar system? Climate of the Past, v. 13, p. 1129–1152, doi:http://dx.doi.org/10.5194/cp-13-1129-2017.

Westerhold, T., and Roehl, U., 2009, High resolution cyclostratigraphy of the early Eocene; new insights into the origin of the Cenozoic cooling trend: Climate of the Past, v. 5, p. 309–327, doi:http://dx.doi.org.ezp3.lib.umn.edu/10.5194/cp-5-309-2009.

Westerhold, T., Roehl, U., Frederichs, T., Bohaty, S.M., and Zachos, J.C., 2015, Astronomical calibration of the geological timescale: closing the middle Eocene gap: Climate of the Past, v. 11, p. 1181–1195, doi:10.5194/cp-11-1181-2015.

Wilf, P., Cúneo, N.R., Johnson, K.R., Hicks, J.F., Wing, S.L., and Obradovich, J.D., 2003, High Plant Diversity in Eocene South America: Evidence from Patagonia: Science, v. 300, p. 122–125, doi:10.1126/science.1080475.

Wing, S.L., Bown, T.M., and Obradovich, J.D., 1991, Early Eocene biotic and climatic change in interior western North America: Geology (Boulder), v. 19, p. 1189–1192, doi:10.1130/0091-7613(1991)019<1189:EEBACC>2.3.CO;2.

Woodburne, M.O., Gunnell, G.F., and Stucky, R.K., 2009, Climate directly influences Eocene mammal faunal dynamics in North America: Proceedings of the National Academy of Sciences of the United States of America, v. 106, p. 13399–13403, doi:http://dx.doi.org.ezp3.lib.umn.edu/10.1073/pnas.0906802106.

Zachos, J.C., Dickens, G.R., Zeebe, R.E., Thorpe, J., Moessinger, J., and VanDecar, J., 2008, An early Cenozoic perspective on greenhouse warming and carbon-cycle dynamics: Nature (London), v. 451, p. 279–283, doi:http://dx.doi.org.ezp2.lib.umn.edu/10.1038/nature06588.

Zachos, J., Pagani, M., Sloan, L., Thomas, E., and Billups, K., 2001, Trends, Rhythms, and Aberrations in Global Climate 65 Ma to Present: Science, v. 292, p. 686, doi:10.1126/science.1059412.

Zhu, J., Poulsen, C.J., and Tierney, J.E., 2019, Simulation of Eocene extreme warmth and high climate sensitivity through cloud feedbacks: Science Advances, v. 5, p. eaax1874, doi:10.1126/sciadv.aax1874.

Zonneveld, J.-P., Gunnell, G.F., and Bartels, W.S., 2000, Early Eocene Fossil Vertebrates from the Southwestern Green River Basin, Lincoln and Uinta Counties, Wyoming: Journal of Vertebrate Paleontology, v. 20, p. 369–386, doi:10.1671/0272-4634(2000)020[0369:EEFVFT]2.0.CO;2.